www.sciencemag.org/content/352/6285/604/suppl/DC1

Supplementary Materials for

Broken detailed balance at mesoscopic scales in active biological systems

Christopher Battle, Chase P. Broedersz, Nikta Fakhri, Veikko F. Geyer, Jonathon Howard, Christoph F. Schmidt,* Fred C. MacKintosh*

*Corresponding author. Email: fcmack@gmail.com (F.C.M.); christoph.schmidt@phys.uni-goettingen.de (C.F.S.)

Published 29 April 2016, *Science* **352**, 604 (2016)
DOI: 10.1126/science.aac8167

This PDF file includes:

Other Supplementary Materials for this manuscript include the following:
(available at www.sciencemag.org/content/352/6285/604/suppl/DC1)

Movies S1 and S2

Supplementary Materials for:

Broken detailed balance at the mesoscale in active biological systems

Authors: Christopher Battle[1,7]*, Chase P. Broedersz[2,3,7]*, Nikta Fakhri[1,4,7]*, Veikko F. Geyer[5], Jonathon Howard[5], Christoph F. Schmidt[1,7,+], and Fred C. MacKintosh[6,7,+]

* Authors contributed equally
+ Corresponding authors

Affiliations:
1 Drittes Physikalisches Institut, Georg-August-Universität, 37077 Göttingen, Germany
2 Lewis–Sigler Institute for Integrative Genomics and Joseph Henry Laboratories of Physics, Princeton University, Princeton, NJ 08544, USA
3 Arnold-Sommerfeld-Center for Theoretical Physics and Center for NanoScience, Ludwig-Maximilians-Universität München, Theresienstrasse 37, D-80333 München, Germany
4 Department of Physics, Massachusetts Institute of Technology, Cambridge, MA 02139, USA
5 Department of Molecular Biophysics & Biochemistry, Yale University, New Haven, Connecticut, USA
6 Department of Physics and Astronomy, VU University, Amsterdam, The Netherlands
7 The Kavli Institute for Theoretical Physics, University of California Santa Barbara, CA 93106, USA

Materials and Methods:

1 Probability flux analysis (PFA)

Here we describe how we analyze experimental time traces to determine probability fluxes in a Coarse Grained Phase Space (CGPS). In general, the raw time traces represent highly stochastic trajectories through phase space, in which case broken detailed balance only becomes apparent when the statistics of transitions between configurations are analyzed over a long time window. Thus we infer a non-zero average flux or current in phase space when the probability for a particular transition in CGPS is unequal to the probability for the reverse transition. The statistical significance of this current is determined through the use of a bootstrapping method described below.

Such statistically non-reciprocal dynamics should be contrasted with the case of deterministic non-reciprocal motion. An example for the latter is the obviously non-reciprocal trajectories of active flagella (*37, 38*) (see also Figure 1), or active swimmers (*39*).

1.1 ***Coarse graining procedure: analyzing continuous time trajectories using discretized low-dimensional projections of phase space*****:** We consider a stationary dynamic system that nevertheless evolves in time on short time scales due to thermal or non-thermal fluctuations or oscillations. Among the set of coordinates that constitute a full specification of the configuration of the system, we observe or track in our analysis D coordinates $x_1, \dots, x_D$. The remaining M coordinates $\tilde{x}_1, \dots, \tilde{x}_M$ are not tracked. Since these coordinates can take on arbitrary values without our knowledge, they will be integrated out below. We, for the moment, only consider spatial or conformational degrees of freedom because momentum in a typical overdamped biological soft-matter system relaxes on time-scales that are much shorter than the temporal resolution of our experiments. For convenience, we have placed a tilde on the degrees of freedom that will be integrated out below.

Our choice of coordinates to describe the configuration of the system is arbitrary, and does not need to correspond, for instance, to the positions of all particles. In general, we can use any complete set of generalized coordinates. These generalized coordinates can be linear or nonlinear functions of the particle positions, via a coordinate transformation. In the main text we consider three cases: (1) where $x_1, \dots, x_D$ are normal mode amplitudes of the flagellum, (2) coordinates of particles coupled through a spring, and (3) the angle and curvature of a cilium. In each case, these can be considered to be functions, e.g., of all the particles in the system. Since these coarse-grained coordinates are independent, they can also be considered to constitute part of a full set of generalized coordinates $x_1, \dots, x_D, \tilde{x}_1, \dots, \tilde{x}_M$ describing the phase space of the system. We note that other variables such as particle concentration or pH may also be used as generalized coordinates of the system.

Since the system is stationary, we can define a probability density that describes how likely it is to find the system in a certain configuration. The dynamics of the system then satisfies the continuity equation:

$$\int_{\Omega} d^D x d^M \tilde{x} \frac{\partial \rho(x_1,\dots,x_D,\tilde{x}_1,\dots,\tilde{x}_M,t)}{\partial t} = -\int_{\partial \Omega} \vec{j} \cdot d\vec{s} \qquad \text{(S1)}$$

where ρ is the probability density and $\vec{j}$ is the current density describing the average motion of the system in the configurational phase space. Here, we consider a region of phase space corresponding to some subset Ω_D of the coordinates that we track $(x_1, \dots, x_D)$. Since we do not track the remaining coordinates $\tilde{x}_1, \dots, \tilde{x}_M$, we thus consider a subset in the full phase space defined by $\Omega = \Omega_D \times \Omega_M$, where Ω_M represents the space spanned by the coordinates $\tilde{x}_1, \dots, \tilde{x}_M$.

Next, we integrate out all but the observed *D* degrees of freedom. The system is then described in terms of the remaining variables by:

$$\int_{\Omega_D} d^D x \frac{\partial \rho(x_1,\dots,x_D,t)}{\partial t} = -\int_{\partial \Omega_D} \vec{j} \cdot d\vec{s} = -\int_{\Omega_D} d^D x \vec{\nabla} \cdot \vec{j}. \qquad \text{(S2)}$$

Here, we have assumed vanishing currents on the boundary $\partial\Omega_M$ of Ω_M, where $\tilde{x}_i = \pm\infty$. Thus, after integrating out all the hidden (untracked) variables, we arrive at a conservation law for a subset Ω_D in the reduced space of variables we track. In principle, since this subset Ω_D is arbitrary, we obtain the following continuity equation in the reduced space of tracked variables,

$$\frac{\partial \rho(x_1,\ldots,x_D,t)}{\partial t} = -\vec{\nabla} \cdot \vec{j}. \tag{S3}$$

Note, in Eqs. (S2) and (S3), the gradient operator and current have dimensionality D, whereas in Eq. (S1) dimensionality is $D + M$, although we use the same symbols. An important implication of this equation is that the divergence of the current field in CGPS must vanish under steady-state conditions (see section 3.9).

A time-trajectory in a two-dimensional ($D = 2$) phase space is depicted schematically in Figure S1. We analyze these trajectories using a discretized coarse-grained representation of phase space, consisting of a collection of $N_1 \times N_2$ equally sized, rectangular boxes, each of which represents a discrete state α (Figure S1B). Such a discrete state in CGPS describes a continuous set of microstates. The dynamics of the system in this two dimensional CGPS satisfies the continuity equation:

$$\frac{dp_\alpha}{dt} = w^{(x_1)}_{\alpha^-,\alpha} - w^{(x_1)}_{\alpha,\alpha^+} + w^{(x_2)}_{\alpha^-,\alpha} - w^{(x_2)}_{\alpha,\alpha^+}, \tag{S4}$$

where p_α is the probability to be in discrete state α. In terms of the probability density above, p_α represents an integral of ρ over the box α. State α has two neighboring states in each direction, resulting in four possible transitions. The rate $w^{(x_1)}_{\alpha^-,\alpha}$ describes the net rate of transitions into state α from the adjacent state α^- upstream from α, i.e., smaller x_1, while $w^{(x_1)}_{\alpha,\alpha^+}$ denotes the rate of transitions from α downstream to α^+ (larger x_1). Similarly, $w^{(x_2)}_{\alpha^-,\alpha}$ and $w^{(x_2)}_{\alpha,\alpha^+}$ denote the upstream and downstream transition rates, respectively, between boxes arranged along the x_2 direction. Note, that these rates have a sign. For example, $w^{(x_1)}_{\alpha^-,\alpha} < 0$ if there are more transitions per unit time from α to α^- (i.e. in the decreasing $x_1$direction) than the reverse.

We estimate these rates from recorded finite-length time trajectories in CGPS by using

$$w^{(x_i)}_{\alpha,\beta} = \frac{N^{(x_i)}_{\alpha,\beta} - N^{(x_i)}_{\beta,\alpha}}{t_{total}}. \tag{S5}$$

Here t_{total} is the total duration of the experimental trajectory and $N^{(x_i)}_{\alpha,\beta}$ is the number of transitions from state α to state β along the direction x_i. In a small fraction of cases in the measured trajectories, the system can go from one box to a non-adjacent box in a single time-

step due to the limited time resolution. For these cases, we perform a linear interpolation of the measured trajectory in CGPS to capture all transition between adjacent boxes.

To plot the current that describes back-and-forth transitions through all four boundaries of the box associated with a discrete state, we define the following current field:

$$\vec{j}(\vec{x}_\alpha) = \frac{1}{2}\begin{pmatrix} w_{\alpha^-,\alpha}^{(x_1)} + w_{\alpha,\alpha^+}^{(x_1)} \\ w_{\alpha^-,\alpha}^{(x_2)} + w_{\alpha,\alpha^+}^{(x_2)} \end{pmatrix}. \quad \text{(S6)}$$

This is the quantity plotted in the probability flux maps. Here, $\vec{x}_\alpha$ is the center position of the box associated with state α. The probability that is plotted in the probability flux maps is estimated from finite-length experimental time series using:

$$p_\alpha = \frac{t_\alpha}{t_{total}}, \quad \text{(S7)}$$

where t_α is the accumulated time that the system spends in state α during the experiment.

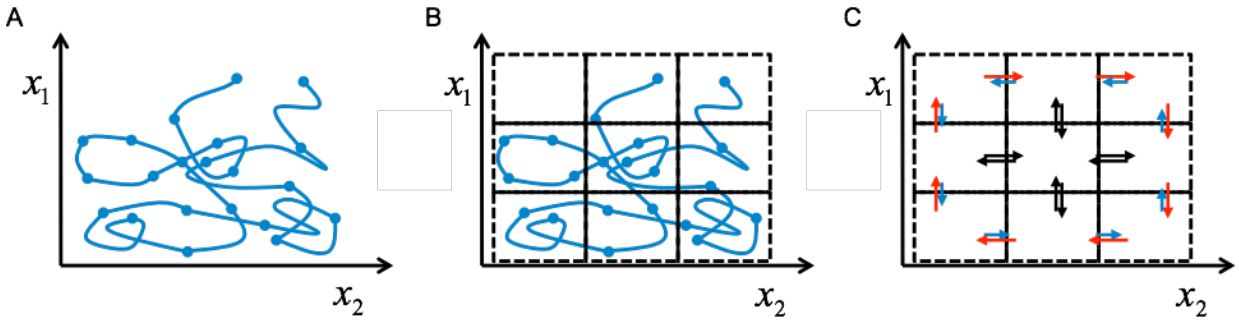

Figure S1 Schematic illustrating the coarse-graining procedure. **A** Trajectory in a phase space spanned by coordinates x_1 and x_2. **B** Grid illustrating the construction of discrete states in phase space. Transitions between neighboring discrete states occur when the system trajectory crosses box boundaries in CGPS. **C** Arrows indicating currents across box boundaries are determined by counting transitions between boxes. In this schematic, the length of the arrows is a measure of the amplitude of the fluxes. Arrows in red correspond to clockwise fluxes and arrows in blue correspond to counter-clockwise fluxes. In this example the arrows in black correspond to transitions which obey detailed balance.

1.2 ***Bootstrapping procedure to determine measurement error:*** The finite length of experimental or simulated trajectories limits the accuracy by which we can estimate fluxes in phase space. The error bars on the probability flux $\vec{j}(\vec{x}_\alpha)$ are determined by counting statistics of the number of transitions in Eq. S5. In general, however, these errors will not be

independent, reflecting correlations between in- and outward transitions for a given box. To estimate the error bars on $\vec{j}(\vec{x}_\alpha)$ more precisely, we bootstrapped trajectories using the experimentally measured or simulated trajectories. To perform this procedure, we first determine the transitions between states from the data and defined the following array

$$A_{data} = \begin{pmatrix} \alpha_1 & \alpha_2 & t_{1,2} \\ \alpha_2 & \alpha_3 & t_{2,3} \\ \dots & \dots & \dots \\ \alpha_N & \alpha_{N+1} & t_{N,N+1} \end{pmatrix}. \quad \text{(S9)}$$

Here, α_i and α_{i+1} are consecutively visited states, and $t_{i,i+1}$ is the amount of time spent in state α_i before transitioning to state α_{i+1}. For example, one can estimate the rate $w_{\alpha^-,\alpha}^{(x_1)}$ from this using:

$$w_{\alpha^-,\alpha}^{(x_1)} = \frac{1}{t_{total}} \sum_k \left(\delta_{\alpha^-,\alpha_{k-1}} \delta_{\alpha,\alpha_k} - \delta_{\alpha,\alpha_k} \delta_{\alpha^-,\alpha_{k+1}} \right). \quad \text{(S10)}$$

The statement that in- and outward transitions are correlated means that pairs of terms in this sum are not independent. For instance, if there is a transition $\alpha^- \longrightarrow \alpha$, contributing to a "count'' in the first term under the sum, then it is likely that this event is followed by a transition $\alpha \longrightarrow \alpha^-$, contributing to a "count" in the second term. If such correlations were not present (i.e., for a Markovian system), we could construct bootstrap trajectories by randomly picking rows from A_{data} (Eq. s9). However, to capture the effects of pairwise correlations between transitions on the accuracy with which we can estimate the fluxes, we bootstrap trajectories (with duration t_{total}) by randomly picking consecutive *pairs* of rows from A_{data}. Empirically, we find that the estimated error bars reduce substantially by including pairwise correlations. Interestingly, this indicates that our systems are not entirely Markovian. It is also possible to probe non-Markovian effects by the use of higher-order correlation functions involving three or more time intervals (*40, 41*).

After producing many bootstrapped realizations of trajectories in CGPS, we can estimate error bars for the currents we determined. For each bootstrapped trajectory we calculate the current field $\vec{j}^{(bs)}(\vec{x}_\alpha)$. By averaging over bootstrap realizations, we estimate the covariance matrix $\mathrm{Cov}\left(j_1^{(bs)}(\vec{x}_\alpha), j_2^{(bs)}(\vec{x}_\alpha)\right)$. To visualize the errorbars (standard error of the mean) on the fluxes, we depict an ellipse aligned with the principle components of this covariance matrix; the long and short radii of these error-ellipses are set by the square roots of the large and small eigenvalues, respectively, of the covariance matrix (Figure S2).

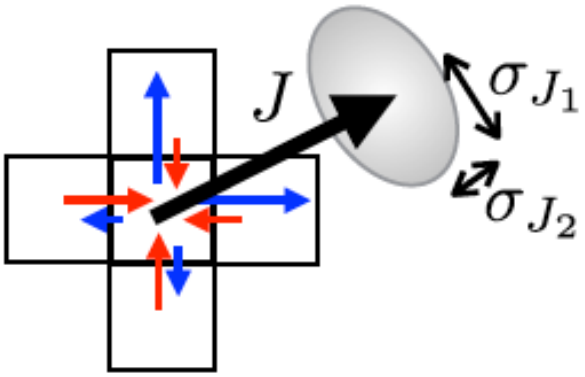

Figure S2 Schematic illustrating the definition of the current field in S6. The flux (black arrow) that we associate with a point at the center of a box is calculated by averaging the inward/outward current contributions from the four boundaries (blue and red arrows) of this box. The confidence intervals are depicted as white, elliptical disks. The axes of these ellipses are aligned with the principle components of this covariance matrix, and their long and short radii are set by the square roots of the large and small eigenvalues, respectively, of the covariance matrix.

1.3 ***Contour integral bootstrapping:*** To quantify the statistical significance of a circulation pattern in phase space, we compute the contour integral along a particular current loop (Figure S3),

$$\Omega = \oint \vec{J} \cdot d\vec{\ell}. \qquad \text{(S11)}$$

This is a measure of the average curl of the current within the contour. It may be possible that errors in estimating the currents are spatially correlated, and this could give rise to spurious loops in CGPS. To investigate the robustness of current loops, we calculate the contour integral Ω for different bootstrap realizations. If the mean of Ω over bootstrap realizations is not significantly different from zero, then the current loop may be spurious.

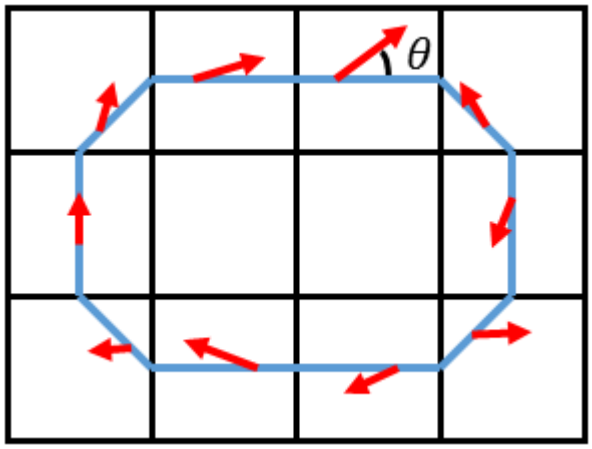

Figure S3*:* Schematic of contour integral. Red arrows correspond to probability current vectors, the blue line depicts the contour integrated around, and θ a representative angle between a current vector and the contour.

1.4 *Brownian dynamics simulations*: The Brownian dynamics simulations model the dynamics of two overdamped, tethered beads with positions X_1 and X_2 coupled by a harmonic spring in 1D. The two beads are in equilibrium with independent heat baths at temperatures T_1 and T_2, as depicted in the main text. The dynamics of this system are described by the equations of motion:

$$\zeta \frac{dx_1(t)}{dt} = k\,(x_2(t) - 2x_1(t)) + \xi_1(t) \text{ and} \qquad \text{(S12)}$$

$$\zeta \frac{dx_2(t)}{dt} = k\,(x_1(t) - 2x_2(t)) + \xi_2(t), \qquad \text{(S13)}$$

where ζ is the drag coefficient on the bead, k is the spring constant (which we chose here to be identical for all three spings), and the white-noise source ξ_i has zero-mean and $\langle \xi_i(t)\xi_j(t')\rangle = 2\,\zeta k_B T_i \delta_{i,j}\delta(t-t')$. This system is only in equilibrium when $T_1 = T_2$. Table S1 gives the numerical values of parameters used in the simulations

Table S1

Parameter	ζ	k_B	k	dt	T_1
Value	18.849	1	1	0.1	1

Figure S4 shows the results of our PFA analysis for two additional cases, not shown in the main text: $T_2 = T_1/2$ and $T_2 = 1.25T_1$. In the former case (left-hand panel), we see strong circulation, as expected, but in the opposite (counter-clockwise) direction to Figure 2C, since bead 1 now has become the "hotter" bead instead of bead 2. In the case $T_2 = 1.25T_1$ (right-hand panel), we see an intermediate case between those presented in the main text in Figure 2. In this case coherent circulation can be seen by eye, but most of the currents are still insignificant, as indicated by their large error discs.

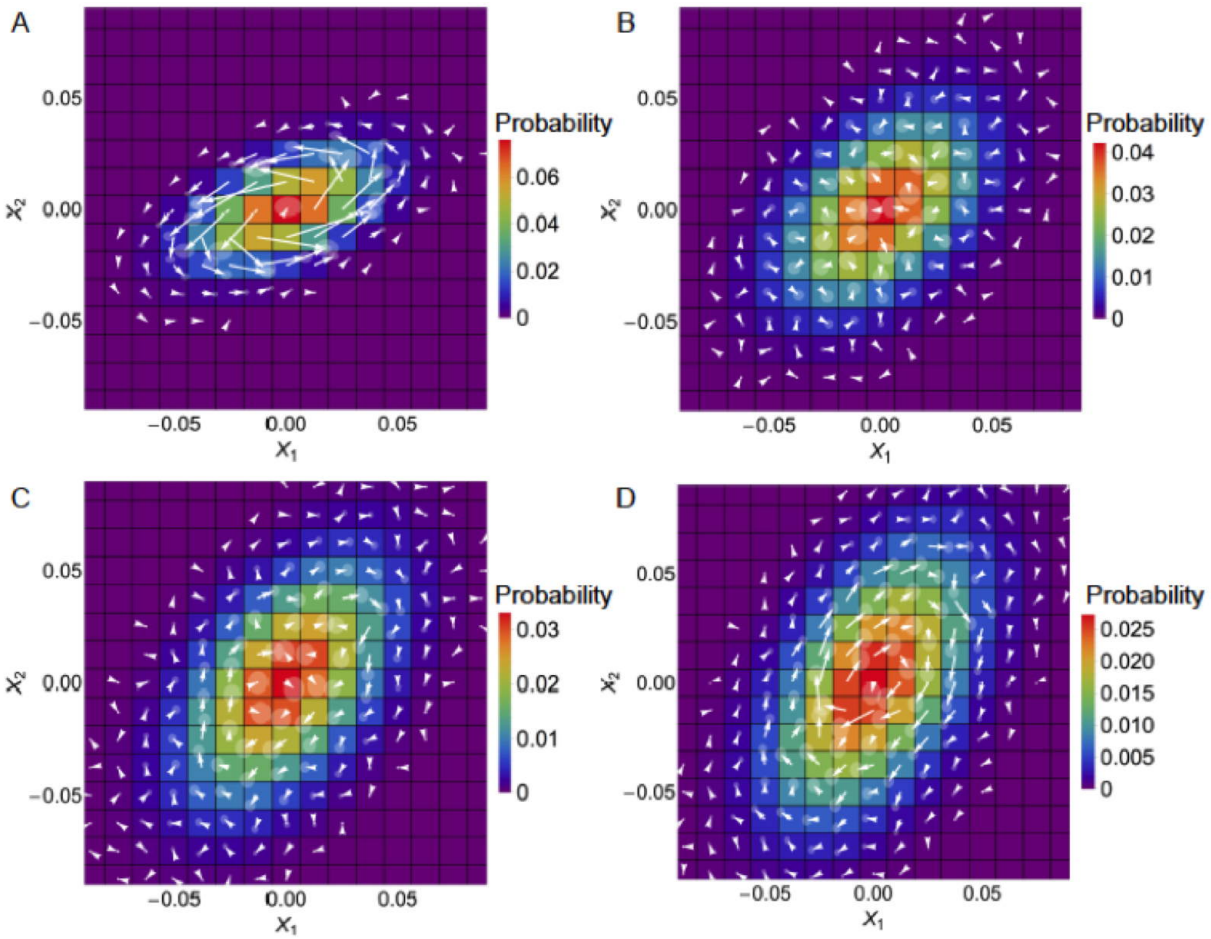

Figure S4*:* Probability and flux maps for the Brownian Dynamics simulations at different temperature ratios. **A**: $T_2 = T_1/2$. **B**: $T_2 = T_1$ (shown also in the main text). **C**: $T_2 = 1.25T_1$. **D**: $T_2 = 1.5T_1$(shown also in the main text). In all cases we simulated trajectories with a total of 10^7 time points using the parameters shown in Table S1.

It is important to note that the currents appearing in the non-equilibrium cases stem from the temperature imbalance between the beads, and do not arise from other heterogeneities in the system, e.g. spring constants. To demonstrate that our results remain valid in heterogonous

systems, we also investigated two-bead model systems in which all three spring constants in the model are different. For this heterogeneous model we confirmed that the system obeys detailed balance using PFA when the temperature of the two beads are equal (Figure S5). By contrast, we find that the heterogeneous model violates detailed balance when the two beads are maintained at different temperatures. This illustrates that heterogeneities in cells or complex materials, such as heterogeneous elastic moduli, do not bias our technique.

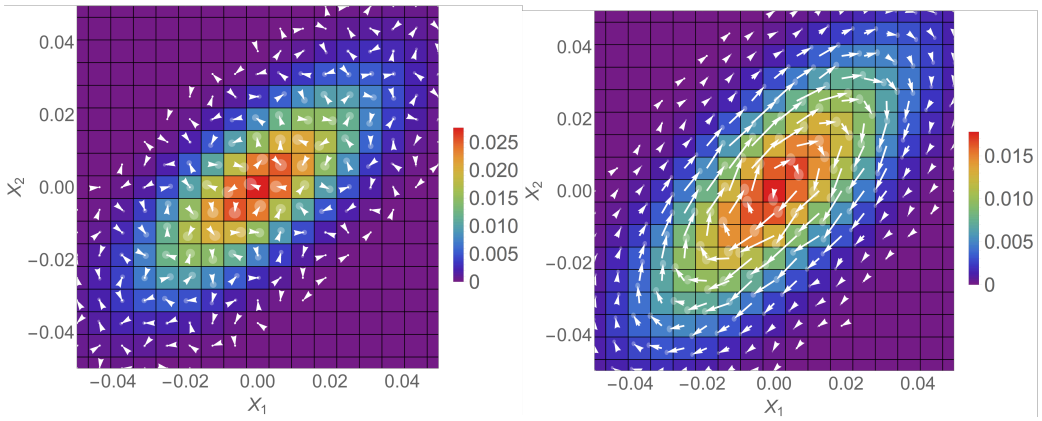

Figure S5: Two-bead spring model with heterogeneity. In this model the 3 springs were chosen to have different spring constants (k_1=1, k_2=5, k_3=2.5, referring to the springs in Figure 2a. The other parameters as in Figure 2). The left panel shows results from our probably flux analysis on a system where the two beads were maintained at the same temperature (T_2=T_1). The right panel shows the results for simulations where T_2=1.5T_1.

There has been some discussion in the literature of using the presence of non-Gaussian fluctuations as a diagnostic for non-equilibrium behavior (*42-44*). While there may be contexts in which such an approach could be insightful, it cannot constitute an unequivocal test of (non-)equilibrium. On the one hand, equilibrium systems can exhibit non-Gaussian fluctuations, e.g., in the presence of anharmonic potentials. On the other hand, non-equilibrium systems can exhibit Gaussian fluctuations. An example of this scenario is provided by the simple two-bead model presented in Figure 2 of the manuscript. Indeed, the distributions of fluctuations for x_1 and x_2 exhibit Gaussian shapes in this non-equilibrium model (See Figure S6). Thus, despite the fact that the two-bead system with differing temperatures (green trace in Figure S6) is out of equilibrium, its fluctuations are Gaussian. Testing for violations of detailed balance, then, gives a conclusive demonstration of non-equilibrium behavior even in the presence of Gaussian

fluctuations. It also avoids the practical difficulties of measuring enough rare "tail" events to conclude non-Gaussianity, and rather analyzes the entire dynamics of the system of interest.

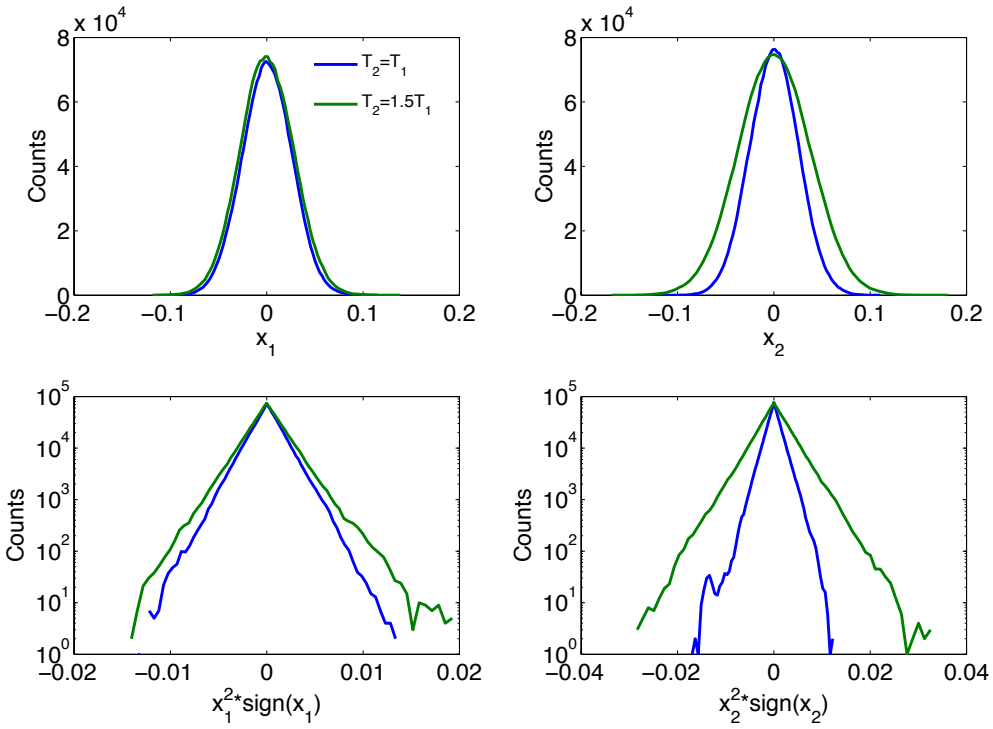

Figure S6: Distributions of fluctuations for the two-bead model in equilibrium (blue) and out of equilibrium (green). In both cases the numerical data are consistent with a Gaussian distribution.

2 Isolated *Chlamydomonas* flagellum

2.1 ***Flagellum preparation:*** All methods used for cell culture, purification and reactivation of flagella are detailed in (*45*). Reagents were purchased from Sigma-Aldrich, St. Louis, MO if not stated otherwise.

In brief, wildtype *Chlamydomonas reinhardtii* cells (CC-125 wild-type mt+ 137c) were grown in liquid Tris-acetate-phosphate (TAP) medium under continuous aeration at room temperature to a final density of approximately 5 x 10^6 cells/ml.

Cells were harvested and deflagellated by the dibucaine procedure. Then the flagella were separated from the cell bodies by centrifugation through a 30% sucrose cushion. Subsequently, the detached flagella were concentrated by centrifugation and demembranated using 1% Igepal.

The buffer used for demembranation was HMDEK (30 mM HEPES, 5 mM $MgSO_4$, 1 mM DTT, and 1 mM EGTA, 50 mM K-acetate, titrated to pH 7.4 with KOH). During the demembranation and for all subsequent steps 0.2 mM Pefabloc was added to all solutions.

The demembranated flagella were reactivated in a buffer HMDEK buffer augmented with, 1% PEG (20k) 1 mM ATP, 1 mM DTT, 10 units/ml creatine kinase and 6.4 mM creatine phosphate.

2.2 ***Imaging chambers:*** Flow chambers were made from double-stick tape and cleaned glass (easy-clean procedure (*46*)) resulting in a chamber with a height of ~100 µm and a width of 3 mm. First, surfaces were blocked with a 2 mg/ml casein solution for 5 minutes, then the sample was placed into the chambers. Finally, the chambers were sealed with VALAP (1:1:1 vasoline:lanolin:parafin).

2.3 ***Microscopy:*** Beating flagella were visualized using phase-contrast microscopy on a Zeiss Axiovert 200 inverted microscope. The microscope was equipped with a 100x Plan-Neofluar NA 1.3 PH3 oil objective, a Zeiss oil phase-contrast condenser (NA 1.4). Additionally a 1.6x Optovar lens was used to enhance sample magnification. The samples were illuminated using a 100-W tungsten lamp. Images were acquired at a frame rate of 1000 fps (frames per second) using a high-speed CMOS camera (Fastcam SA3, Photron) with an effective pixel size of 106.25 nm x 106.25 nm.

2.4 ***Flagellum tracking and normal modes:*** The backbone of the flagellum was tracked using Fluorescence Image Evaluation Software for Tracking and Analysis (FIESTA) (*47*). The shape of the flagellum was parametrized by the tangent angle $\theta(s) = du\, d\!s$ at every point *s* along the arc length of the flagellum, ($0 < s < L$), where L is the contour length of the flagellum. This shape was then decomposed into the appropriate set of dynamic normal modes for an elastic filament with unconstrained ends in a viscous medium. The normal modes are given by (*48*):

$$\psi_n(s) = \frac{\sqrt{L}}{k_n}\left(\frac{\sin(k_n s/L)}{\cos(k_n/2)} + \frac{\sinh(k_n s/L)}{\cosh(k_n/2)}\right) \qquad \text{(S14)}$$

for *n* = 1,3,5,…. For even *n,* the modes are similar, with cos replacing sin and cosh replacing sinh in the numerator and sin replacing cos and sinh replacing cosh in the denominator. Here $k_n \cong (n+1/2)\pi$ is the wave vector. The mode amplitudes can be obtained from:

$$a_n(t) = -\int \psi_n(s')\theta(s',t)\,ds' \qquad \text{(S15)}$$

Supplementary movie

Movie S1: A beating flagellum from *Chlamydomonas reinhardtii*, acquired at 1000 Hz.

3 Cilium

3.1 Cell culture: Madin-Darby canine kidney (MDCK-II) cells (a kind gift from Andreas Janshoff) were cultured in Minimum Essential Medium with 2 mM L-glutamine, 1% penicillin-streptomycin, and 10% fetal bovine serum added. Cells were grown to confluence on poly-L-lysine-coated polycarbonate membranes (PCMs), and experiments were performed 1 - 2 days after full confluence (5 - 7 days after seeding).

3.2 Blebbistatin treatment: Blebbistatin was added to the culture medium of confluent cells to a concentration of 50 µM of the active (-) enantiomer (100 µM of racemic solution, CalBiochem, 203389). The cells were incubated in the blebbistatin solution at 37°C for 30 minutes, after which they were mounted with blebbistatin-containing medium in viewing chambers for video-tracking experiments.

3.3 Imaging chambers: Imaging chambers for the cilium experiments were constructed out of a microscope slide and a coverslip sealed together on all sides with extra-thin double stick tape, creating a chamber approximately 80 µm in height. Cells on PCMs were folded over for side-viewing as described in (*49*). PCMs were mounted in the chamber with approximately 50 µl of medium. Figure S5 shows a schematic of the experimental geometry.

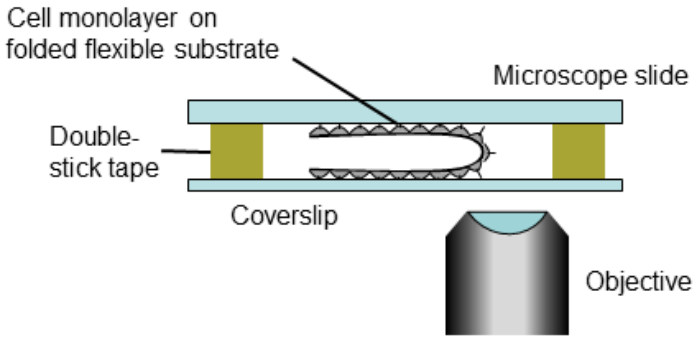

Figure S7: Schematic of imaging chamber and experimental geometry.

3.4 Microscopy: Primary cilium experiments were performed using a custom-built DIC/optical-trapping setup described elsewhere (*50*). Images were acquired with an MTI VE1000 analog camera (DAGE-MTI, Michigan City, IN) at a rate of 25 Hz and read out via a frame grabber card and a custom-written LabView VI.

3.5 Tracking: The backbones of primary cilia were extracted from the differential interference contrast (DIC) micrographs using a custom MATLAB algorithm. Backbones were tracked using a Canny edge-filtering scheme combined with the geometric mean filter described in (*49, 51*) to further enhance the line signal. The backbones were then smoothed by linearly interpolating after rejecting outliers. Points on the cilium backbone were considered to be outliers when the displacement between consecutive frames exceeded a maximal interframe distance constraint (typically $\sim$ 500 nm). Figure S6B shows a typical example of such a backbone fit.

3.6 Fitting: Angle and curvature coordinates were obtained by a two-step fitting process to enhance robustness against perturbations due to systematic tracking failure at the tip (i) and base of the cilium (ii); (i) is due to tip excursions out of the focal plane and (ii) is due to scattering from the cell monolayer/polycarbonate membrane. The angle at the base of the cilium was determined from the slope of a linear fit to the lower 25% of the cilium. The curvature of the cilium was determined from the coefficient of the quadratic term in a 2^{nd} order polynomial fit to as much of the cilium contour length as possible (typically 70 - 80%). Tracking errors may result in spurious, large local distortions in the backbone of the cilium, which can introduce errors in the determination of slope and curvature. To correct for this, the residuals of the quadratic fit were calculated, as well as the standard deviation of the residual distribution. The linear and quadratic fits were then recalculated, ignoring points with residuals greater than three standard deviations away from the residual mean. Empirically, we found that this corrects for most spurious local distortions in the cilium backbone due to tracking errors. Figure S6 shows an example of a typical fit.

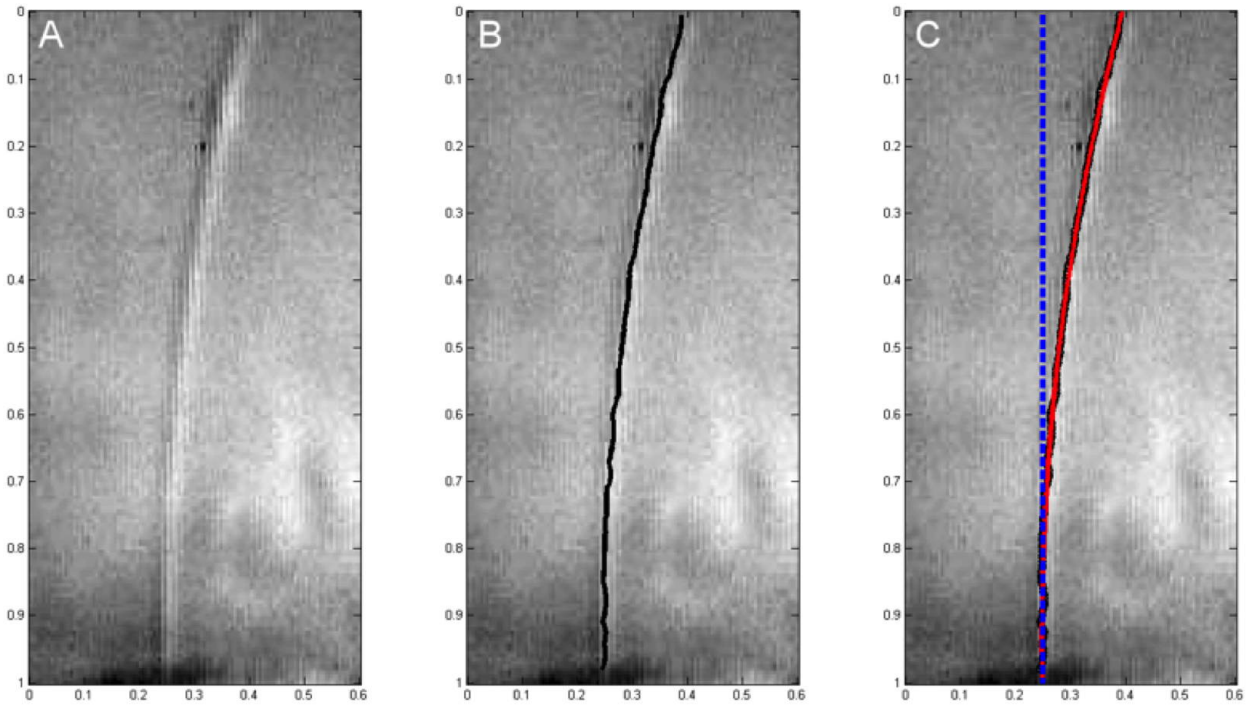

Figure S8: Cilium micrograph with fitted backbone, curvature, and angle. **A**: Micrograph of a cilium. **B**: Backbone determined by the tracking algorithm (black) overlaid on the cilium. **C**: Curvature (red) and basal angle (blue) fits overlaid on B.

In most cases, the final angle and curvature time series were not uninterrupted trajectories. This is due to the fact that in the course of an entire movie ($\sim$1 hr), the cilium sometimes moved out of focus. We were left then with a series of shorter trajectories of varying lengths. Not-a-number (NaN) values were inserted in these breaks in the time series. When PFA is performed on a time series with NaN values, a box containing the end of a trajectory has an incoming transition counted, but no transition out, and a box containing the start of a trajectory has a transition out counted, with no corresponding transition in. They were typically on the order of 20 individual trajectories that make up the time series reported here.

3.7 Angle/curvature histograms: Figure S7 shows angle/curvature histograms for the untreated and blebbistatin-treated cilia shown in the main text (Fig 3C, E, respectively). Distributions have their means subtracted, as they have for the analysis in the main text. Blebbistatin treatment induced a significant narrowing of the distributions of both curvature and angle, though the effect is more pronounced for the angle.

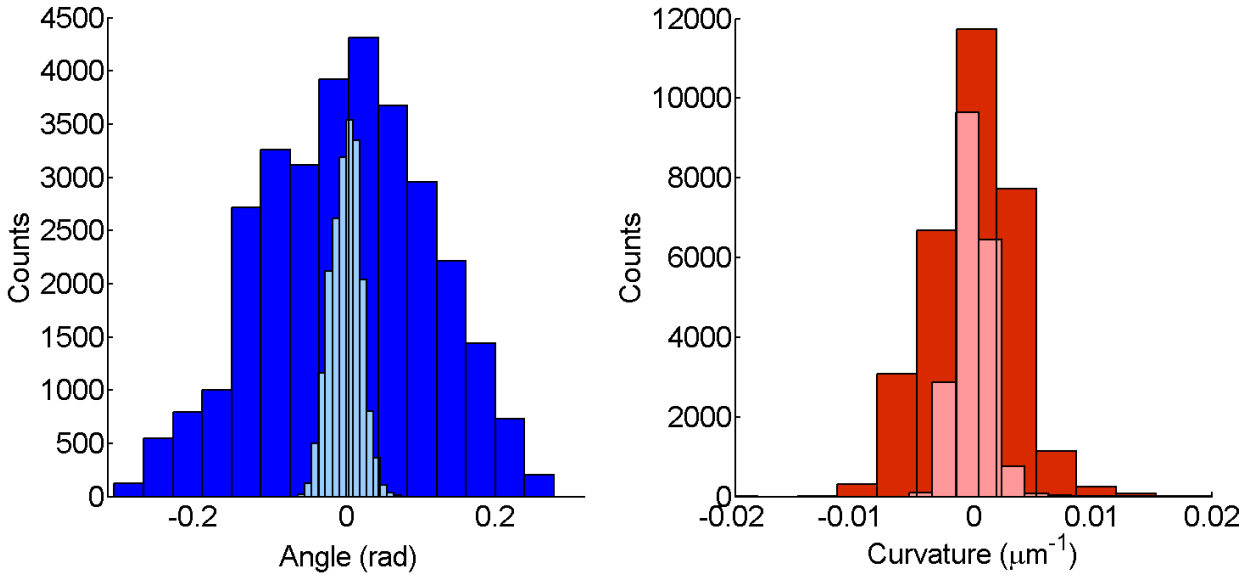

Figure S9: Angle and curvature histograms for the untreated and blebbistatin-treated cilia in the main text (Fig 3C, E, respectively). The left-hand panel shows the distribution of angles for the untreated (blue) and blebbistatin-treated (light blue) cilia. The right-hand panel shows the distribution of curvatures for the untreated (red) and blebbistatin-treated (light red) cilia.

3.8 Flow tests: To control for flow in the sample chamber, we tracked diffusing background particles at various points in the movie recorded with the untreated cilium. Tracking was performed using the SpotTracker plugin (*52*) for ImageJ, after edge filtering and Gaussian smoothing (5 pixel width) the images in ImageJ. We only tracked particles with trajectories of at least 100 frames (4 s) that were easily visible in DIC. The inset in Figure S10 depicts one such particle. These particles had a diameter between 1 and 1.5 microns, as estimated from the images with a calibrated pixel scale, and 12 particles were tracked for a total of 13 trajectories (one that diffused out-of-frame then back in, making it possible to track its trajectory starting at two different times). Figure S10 shows histograms of diffusion coefficients for the particles' *x* (parallel to cilium axis, blue) and *y* (perpendicular to cilium axis, red) trajectories. The blue and red lines mark the means of the *x* and *y* distributions, respectively. The distributions of the two coordinates' diffusion coefficients have comparable means, as expected in the case of no flow in the chamber. The chamber is asymmetric (~ 60 x 20 mm), with the long axis corresponding to the *y* coordinate. Flows along this direction would be expected to have the most influence on cilium motion. The theoretical diffusion coefficient for a sphere in an aqueous solution is given by:

$$D = k_B T / 6\pi\eta a \qquad \text{(S16)}$$

where *D* is the sphere's diffusion coefficient, k_B is Boltzmann's constant, *T* is temperature, η is the viscosity of the solvent, and *a* is the sphere's radius. The black line in Figure S10 shows *D* for a 1.25 μm diameter sphere at 20°C. This corresponds to the average size of the tracked particles and may represent a systematic underestimate of the diffusion constant because of a systematic overestimation of the size of the particles, due to diffraction and distortions from the DIC imaging.

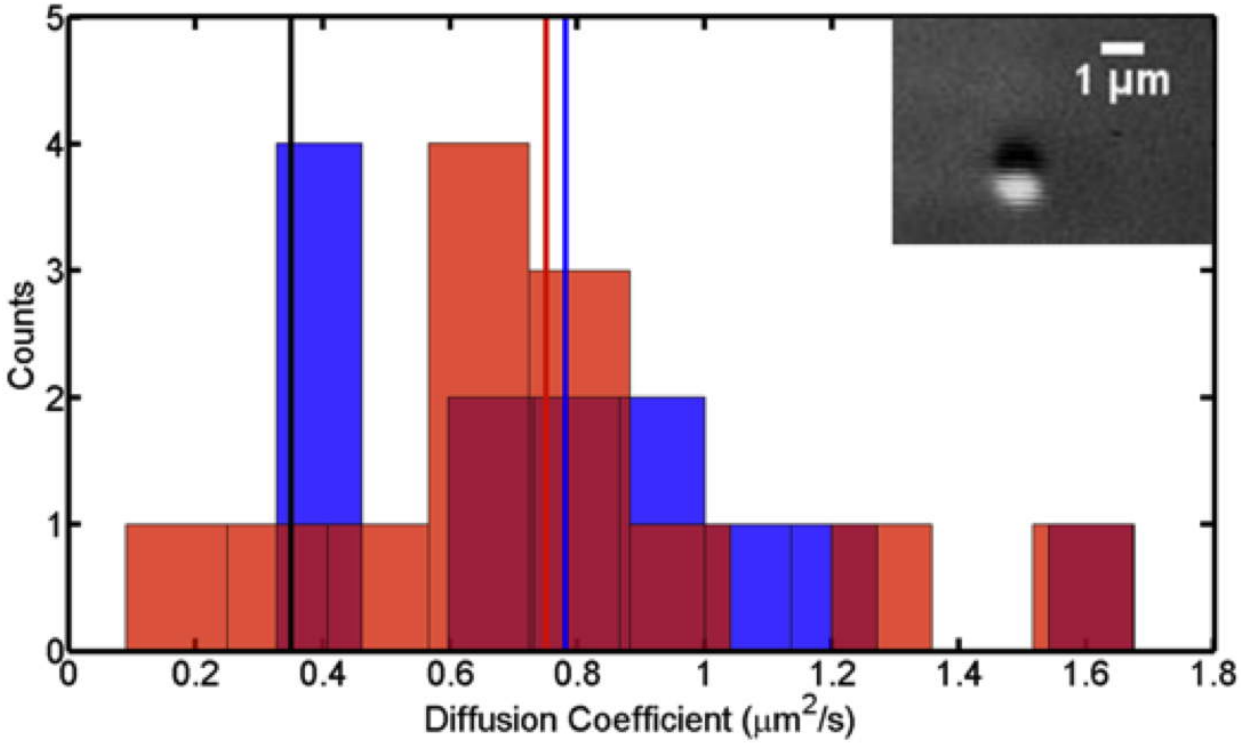

Figure S10: Histograms of diffusion coefficients for the tracked particles in the *x*- and *y*-directions. Distributions of diffusion coefficients in *x* (blue) and diffusion coefficients in *y* (red) are comparable. The blue line shows the mean of the diffusion coefficients in *x* and the red line the mean of the diffusion coefficients in *y*. The black line shows the expected diffusion coefficient for a sphere 1.25 μm in diameter in water at 20° C. Inset: Micrograph of one of the tracked particles.

To set an upper bound on background flow in the sample, we performed Brownian dynamics simulations on ensembles of beads with the same trajectory lengths and diameters as the particles measured. Figure S11 shows histograms of the mean displacement for a lag time of 1 s of the trajectories obtained for simulations with no background flow (blue) and 200 nm/s background flow (red). The black line indicates the mean *y*-displacement of the ensemble of particles that we measured. Comparing data to simulations, we can exclude background flows of 200 nm/s or greater in our sample with a 95% confidence level given the mean of our data

and the simulated data. The drag force on a cylinder of the cilium's dimensions from 200 nm/s flow would be 0.2 fN/µm. A transverse point force of 0.2 fN on the tip of a fixed elastic rod with the cilium's bending stiffness (3 x 10^{-23} Nm^2) (*49, 53, 54*) and length (14 µm) would result in nanometer displacements, well below the excursions that we can resolve. Thus, we do not expect that the measured dynamics of the cilium resulted from background flows in the sample chambers.

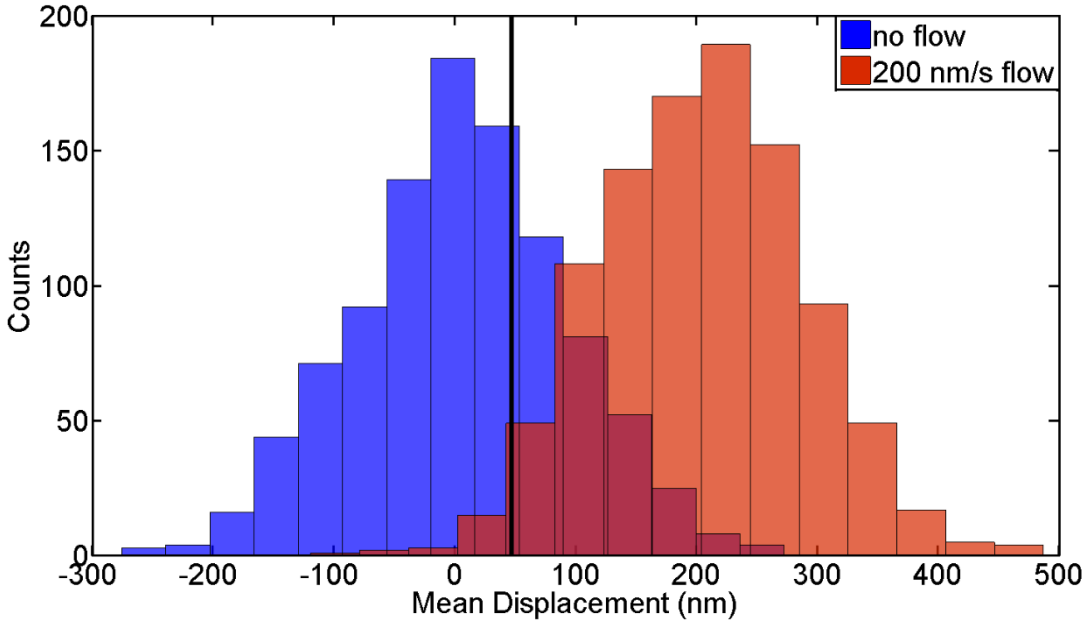

Figure S11: Histograms of means of simulated mean displacements at a lagtime of 1 second. The blue distribution corresponds to simulated particles without flow while the red distribution corresponds to simulated particles in 200 nm/s flow. The black line depicts the mean of the distribution of mean displacement at a 1 s lagtime of the experimental data.

Finally, to control for possible stochastically varying background currents in the sample, we performed a cross-correlation analysis on the *y*-position of the cilium and the tracked particles' *y*-positions. Since the particle trajectories are relatively short (100-500 time steps), it is possible that individual trajectories exhibit high cross-correlations by chance. However, the average of the cross-correlation functions should lie close to zero, unless the motion of the particle and cilium are both driven by the same flow. Figure S12 depicts the various individual cross correlation functions (gray) and the average (red). We find that the average cross-correlation lies close to zero, as expected for uncorrelated motions. Additionally, the *x*- and *y*-diffusion coefficients have similar means, which also indicates that there are no significant stochastically varying fluid flows along the *y*-direction.

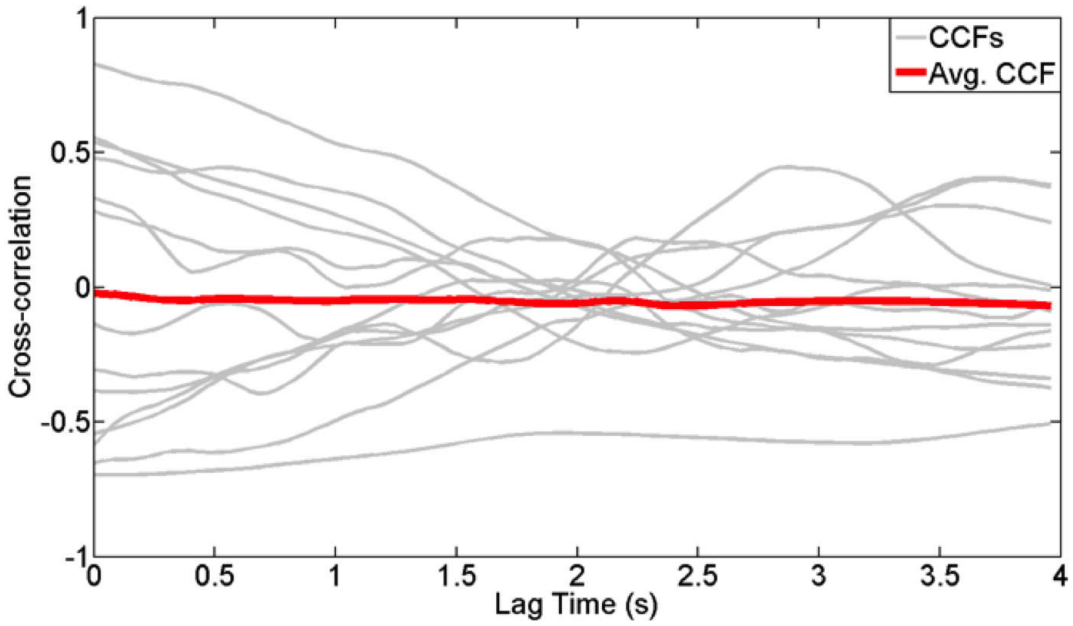

Figure S12: Cross-correlation functions of cilium and particle *y*-trajectories. The gray traces show the cross-correlation functions of the cilium and individual particles, while the red line shows their average.

3.9 Steady state test: Our definition of steady state is a relative one, based on a separation of time scales. In a strict sense, no cell or part of a cell such as the cilia of MDCK cells, will remain in a true steady state indefinitely. Eventually, the cells will deconstruct their cilia when going through mitosis, go into a dormant state, or die. Our analysis focuses on dynamic processes that happen on time scales much shorter than those slow changes in cell fate. We verified that the systems we studied remained in an approximate steady state during our selected time windows. To this end we inspected the divergence of the fluxes in phase space, inferred from the experimental trajectories. The continuity equation (Eq. S3) implies that the divergence of the fluxes should vanish in steady state. Thus, to demonstrate that our experimental time trajectories correspond to steady-state conditions, we computed the divergence of the divergence of the fluxes for the primary cilia of MDCK cells that we analyzed in this paper, and confirmed that these divergences are zero (within error bars). As an example, we show in Fig. S13 the divergence of the flux field of the primary cilia data shown in Fig. 3C of the main text.

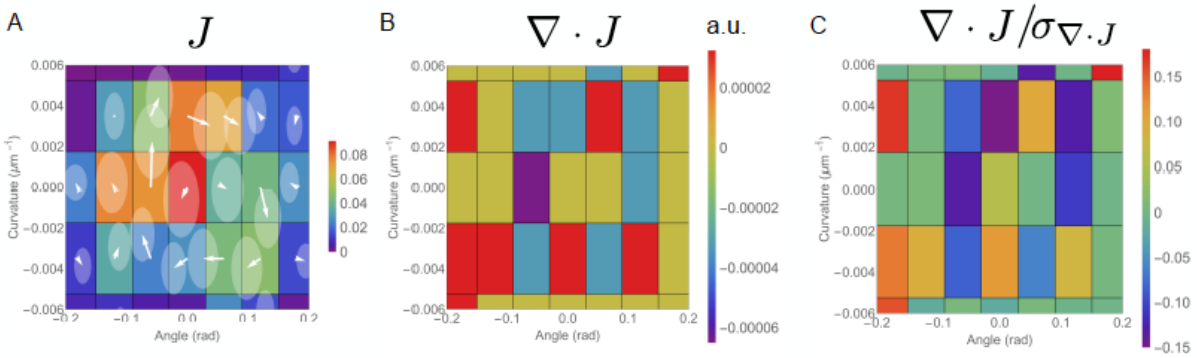

Figure S13: A) Fluxes in a configurational phase space of angle and curvature of a primary cilium (from Fig. 3C), B) map of the divergence of the fluxes in A) and C) the divergence of the fluxes normalized by the corresponding standard error. The small values (less than one) of the ratio of the divergence of the current to its standard error serve as a consistency check on our analysis together with the absence of significant drift of the system over the observed time window.

3.10 Additional untreated cilia: In addition to the two untreated cilia shown in the main text (Fig. 3C,D), we here analyzed the dynamics of two more untreated cilia to illustrate sample-to-sample variations. Figures S14A and S15A show the angle distributions for these cilia. Both of the distributions are multi-modal, reflecting additional slow dynamics in the mean cilium position. Since acquiring adequate statistics on such dynamics would require measuring for prohibitively long times, we high-pass filtered the angle and curvature trajectories of both cilia by subtracting a running average over a symmetric time window (of size 64 and 80 seconds) from the measured signal, respectively. Figures S14B and S15B shows the results of PFA on these cilia. As in the case of the cilia presented in the main text, significant currents are present in each case. Clockwise currents are apparent in both of the flux maps. To test the significance of these patterns, we bootstrapped the contour integrals of the currents around the paths along the dashed white lines, obtaining the histograms shown in Figs. S14C and S15C. The histograms show a signal-to-noise ratio Ω/σ_Ω (see Fig. S3) of 1.73 and 1.83 respectively, indicating a non-zero mean of the current contour integral with a normal confidence interval of > 95% (p = 0.042 and 0.034, respectively).

.

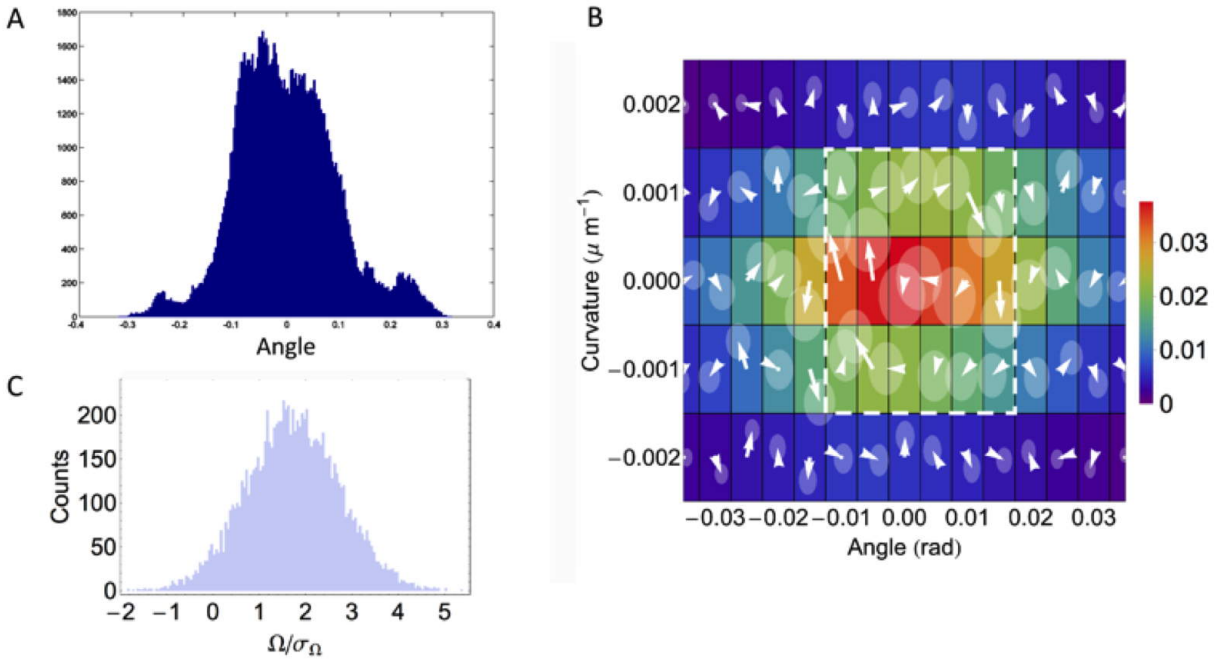

Figure S14*:* Analysis of an additional untreated cilium #1. **A**: Angle distribution. **B**: Probability distributions (color map) and probability flux map (white arrows) from PFA. The translucent discs represent the 2-sigma confidence interval of the probability current distribution obtained from bootstrapping. Data were high-pass filtered with a window size of 64 seconds. The dashed white box indicates the contour integrated around in C. **C**: Normalized contour integral distribution, with a mean centered on 1.73.

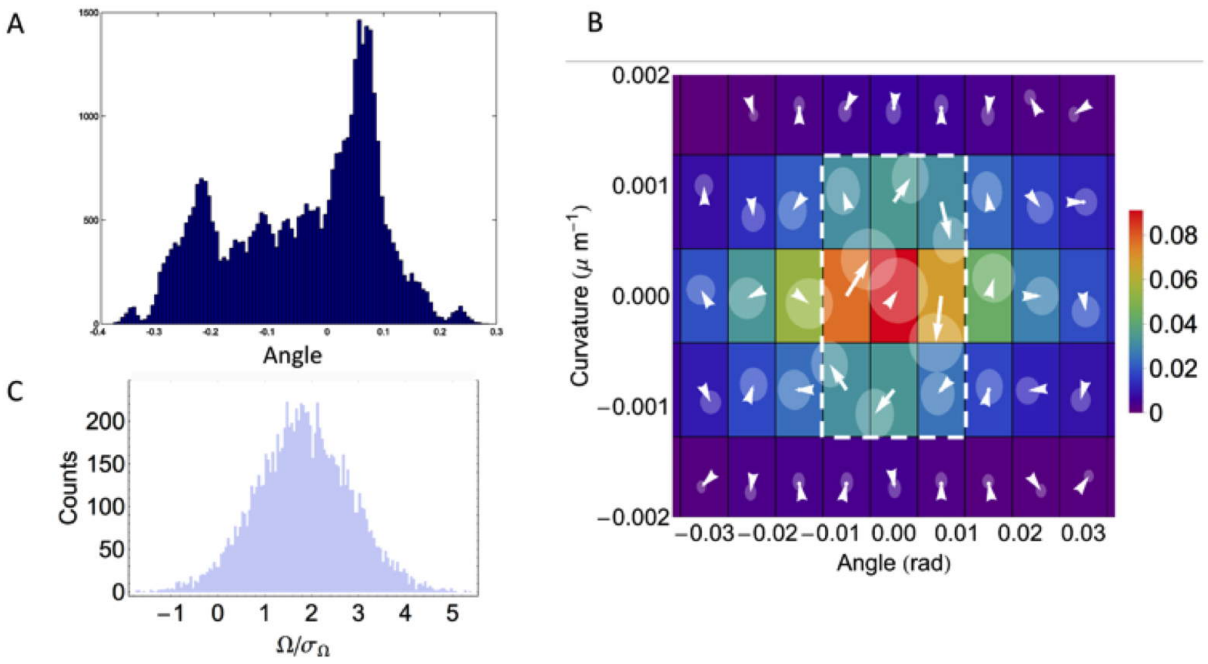

Figure S15*:* Analysis of additional untreated cilium #2. **A**: Angle distribution. **B**: Probability distributions (color map) and probability flux map (white arrows) from PFA. The translucent discs represent the 2-sigma confidence interval of the probability current distribution obtained from bootstrapping. Data were high-pass filtered with a window size of 80 seconds. The dashed white box indicates the contour integrated around in C. **C**: Normalized contour integral distribution, with a mean centered on 1.83.

3.11 ATP-depleted cilium: To explore the effects on the breaking of detailed balance of suppressing cellular activity, we recorded cilium dynamics on cells depleted of adenosine triphosphate (ATP). To deplete ATP, cells were incubated in glucose-free Dulbecco's MEM solution for 3 hours at 37°C prior to the experiment. After the initial glucose-free incubation, Antimycin A and 2-Deoxy-D-glucose were added to the cells' culture medium to a concentration of 10 µM and 10 mM, respectively. The cells were then incubated for 10 - 15 minutes at 37°C. After the final incubation step, the cells were mounted in the glucose-free, Antimycin A and 2-Deoxy-D-glucose containing solution for the experiments. Figure S16A depicts the angle (blue) and curvature trajectories (red) for a cilium on a cell depleted of ATP. The amplitudes of the angle and curvature fluctuations were sharply curtailed in comparison to the non-depleted cells, similar to the blebbistatin-treated case described in the main text. In addition, the slow dynamics in the angle leading to multi-modal distributions were not present in the ATP-depleted cells. Figure S16B shows the results of PFA on these trajectories. Almost all the arrows have magnitudes smaller than the radius of their error discs, indicating a lack of significant currents. Despite this fact, a counter-clockwise current, enclosed by the dashed white box, is still apparent in the flux map. To test whether this pattern was statistically significant or not, we bootstrapped the contour integral around it, obtaining the histogram shown in Figure S16C. The

bootstrapped contour integral distribution is centered at 0.98, indicating marginal (p = 0.16) significance (Note: Positive values here are defined as counter-clockwise circulation, in contrast to the preceding section).

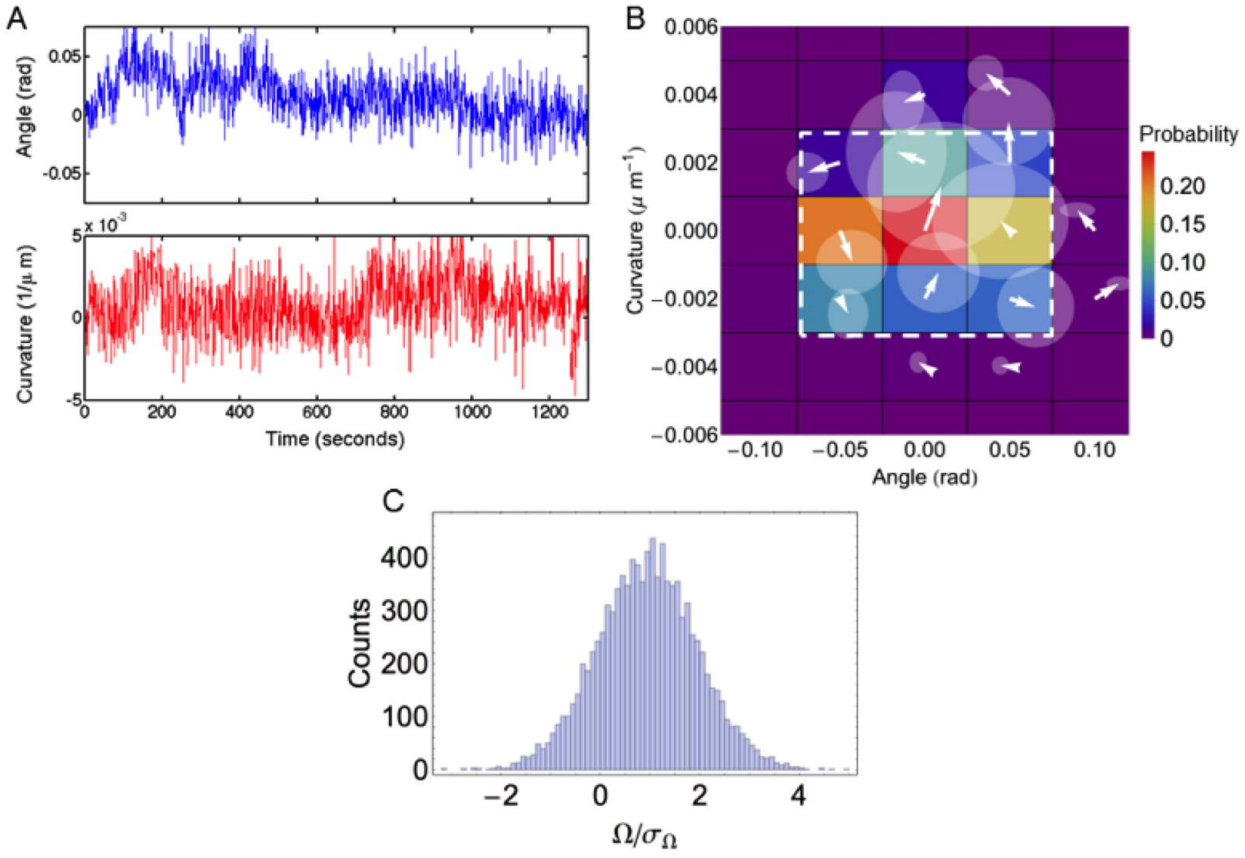

Figure S16*:* Analysis of an ATP-depleted cilium. **A**: Angle (blue) and curvature (red) trajectories. **B**: Probability distributions (color map) and probability flux map (white arrows) from PFA. The translucent discs represent a 2-sigma confidence interval of the probability current distribution, obtained by bootstrapping. The dashed white box indicates the contour integrated around in C. **C**: Normalized contour integral distribution, with a mean at 0.98.

Supplementary Movie:

Movie S2: DIC video recording of primary cilium fluctuations acquired at 25 Hz. Movie down-sampled to 0.2 Hz, with playback frame rate of 50 Hz (sped up 250x).

4 Microtubule fluctuations, equilibrium control

4.1 ***Microtubule preparation:*** Microtubules were polymerized at 37°C in BRB80 buffer (80 mM K-Pipes, pH 6.8, 1 mM EGTA, 1 mM MgCl2) augmented with 5 mM MgCl2, 1 mM GTP , 20 µM unlabeled Tubulin and 5% DMSO for 40 min. Microtubules were then spun into a pellet in an Beckmann tabletop airfuge for 5 min at 25 psi. The pellet was resuspended in 100 µl of BRB80 buffer containing 10 µM taxol, that was filtered using a 0.22 µm filter. All reagents were purchased from Sigma Aldrich.

4.2 ***Sample chambers:*** For imaging, freshly resuspended microtubules were diluted 40x in taxol containing BRB80 buffer augmented with 0.1 mg/ml Casein. 7 µl of this solution were pipetted onto a microscopy slide and covered with a 22x22 mm cover glass. The chamber height was between 1-3 µm and it was sealed using Valap, a 1:1:1 mixture of lanolin, paraffin, and petroleum jelly, heated to 70°C. The glass was pre-cleaned by 15 min sonication steps in 5% Mucasol solution and ethanol followed by an extensive washing step using filtered double-distilled water and a drying step using pressurized nitrogen.

4.3 ***Microscopy:*** Microtubules were visualized by darkfield microscopy in a Nikon Eclipse Ti microscope using a Nikon Plan Fluor 100x, NA 0.5-1.3 lens and a Nikon oil darkfield condenser NA 1.43-1.20. The sample was illuminated with a Sola light engine (lumencor). Fluctuating microtubules were imaged for 10 min using a Andor Zyla 4.2 camera (2x2 binning). The exposure time was 5 ms, the effective pixel-size 128 nm/pixel.

4.4 ***Analysis of microtubule fluctuations:*** As a negative control of our method when applied to an equilibrium system, we tracked the transverse thermal bending fluctuations of an 85 µm long microtubule over 5.5 minutes. Figure S18A and B show time traces of the first two bending modes, while Fig. S18C depicts the results of PFA on these trajectories. As in the case of the ATP-depleted and blebbistatin-treated cilia, the majority of arrows have magnitudes smaller than the radius of their error discs, indicating a lack of significant currents. Additionally, we tested whether the noisy clockwise current enclosed by the dashed white box was significant by bootstrapping its contour integral as previously described. The resulting histogram, shown in Fig. S17D, is centered at 0.64, indicating a marginal ($p = 0.26$) significance of the circulation pattern.

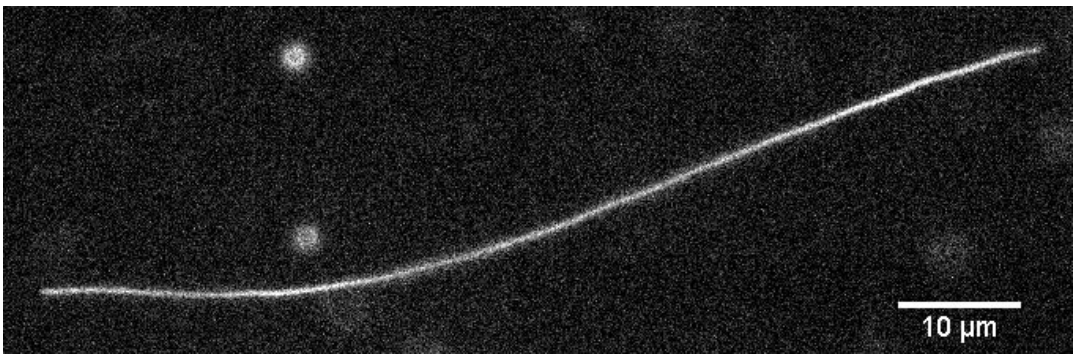

Figure S17 Taxol-stabilized microtubule imaged using dark field microscopy. The exposure time was 5 ms, the length of the microtubule 85 µm. The movie of 1000 frames acquired at 3 Hz was analyzed.

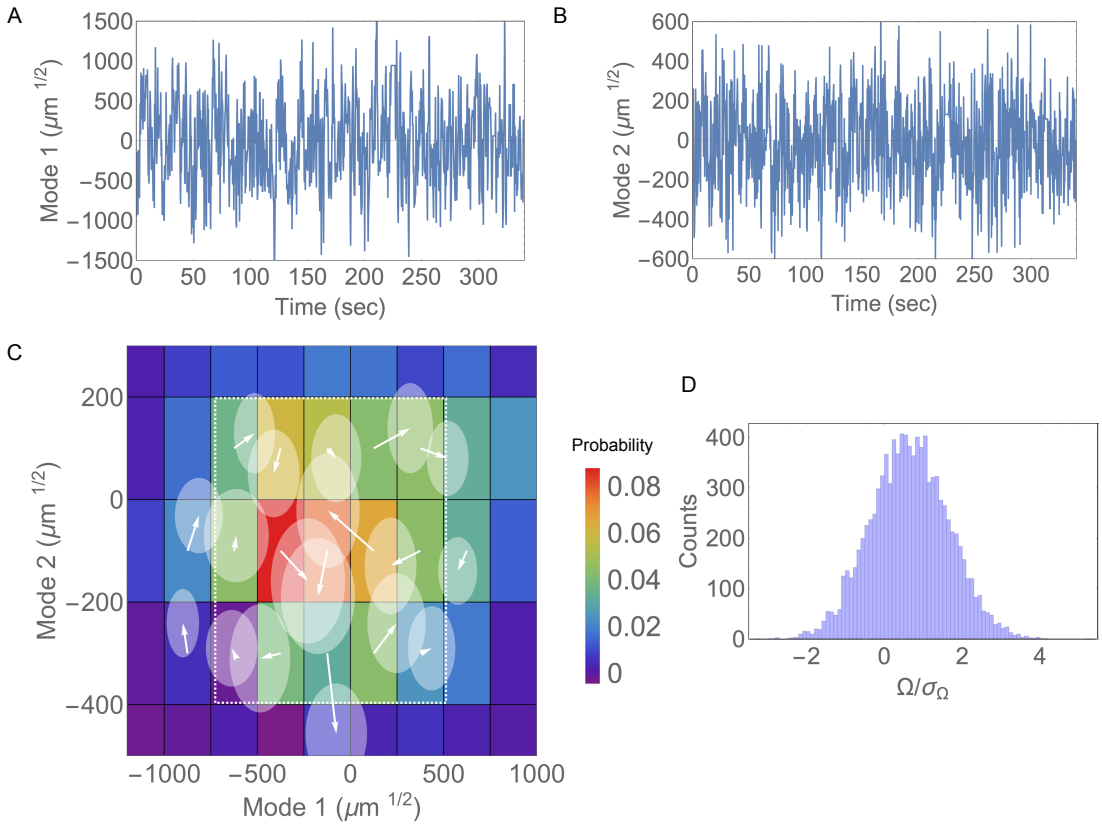

Figure S18: Thermal microtubule fluctuations. A-B) Time series of 1st mode (A) and 2nd mode (B) microtubule fluctuations at room temperature. C) Probability distributions (color map) and probability flux map (white arrows) from PFA. The translucent discs represent a 2-sigma confidence interval of the probability current distribution obtained from bootstrapping. The dashed white box indicates the contour integrated around in D. D) Normalized contour integral distribution, with a mean at 0.64.

References and Notes

1. L. Boltzmann, *Sitzungsberichte Akad. Wiss., Vienna, part II* **66**, 275–370 (1872).

2. B. Alberts, A. Johnson, J. Lewis, M. Raff, K. Roberts, P. Walter, *Molecular Biology of the Cell* (Garland Science, New York, ed. 5, 2007).

3. C. P. Brangwynne, G. H. Koenderink, F. C. MacKintosh, D. A. Weitz, Cytoplasmic diffusion: Molecular motors mix it up. *J. Cell Biol.* **183**, 583–587 (2008). doi:10.1083/jcb.200806149 Medline

4. N. Fakhri, A. D. Wessel, C. Willms, M. Pasquali, D. R. Klopfenstein, F. C. MacKintosh, C. F. Schmidt, High-resolution mapping of intracellular fluctuations using carbon nanotubes. *Science* **344**, 1031–1035 (2014). doi:10.1126/science.1250170 Medline

5. M. Guo, A. J. Ehrlicher, M. H. Jensen, M. Renz, J. R. Moore, R. D. Goldman, J. Lippincott-Schwartz, F. C. Mackintosh, D. A. Weitz, Probing the stochastic, motor-driven properties of the cytoplasm using force spectrum microscopy. *Cell* **158**, 822–832 (2014). doi:10.1016/j.cell.2014.06.051 Medline

6. J. J. Hopfield, Kinetic proofreading: A new mechanism for reducing errors in biosynthetic processes requiring high specificity. *Proc. Natl. Acad. Sci. U.S.A.* **71**, 4135–4139 (1974). doi:10.1073/pnas.71.10.4135 Medline

7. H. C. Berg, E. M. Purcell, Physics of chemoreception. *Biophys. J.* **20**, 193–219 (1977). doi:10.1016/S0006-3495(77)85544-6 Medline

8. M. E. Cates, Diffusive transport without detailed balance in motile bacteria: Does microbiology need statistical physics? *Rep. Prog. Phys.* **75**, 042601 (2012). doi:10.1088/0034-4885/75/4/042601 Medline

9. G. Lan, P. Sartori, S. Neumann, V. Sourjik, Y. Tu, The energy-speed-accuracy tradeoff in sensory adaptation. *Nat. Phys.* **8**, 422–428 (2012). doi:10.1038/nphys2276 Medline

10. B. Nadrowski, P. Martin, F. Jülicher, Active hair-bundle motility harnesses noise to operate near an optimum of mechanosensitivity. *Proc. Natl. Acad. Sci. U.S.A.* **101**, 12195–12200 (2004). doi:10.1073/pnas.0403020101 Medline

11. S. C. Weber, A. J. Spakowitz, J. A. Theriot, Nonthermal ATP-dependent fluctuations contribute to the in vivo motion of chromosomal loci. *Proc. Natl. Acad. Sci. U.S.A.* **109**, 7338–7343 (2012). doi:10.1073/pnas.1119505109 Medline

12. D. A. Egolf, Equilibrium regained: From nonequilibrium chaos to statistical mechanics. *Science* **287**, 101–104 (2000). doi:10.1126/science.287.5450.101 Medline

13. R. Zia, B. Schmittmann, Probability currents as principal characteristics in the statistical mechanics of non-equilibrium steady states. *J. Stat. Mech.* **2007**, P07012 (2007). doi:10.1088/1742-5468/2007/07/P07012

14. E. M. Purcell, Life at low reynolds number. *Am. J. Phys.* **45**, 3–11 (1977). doi:10.1119/1.10903

15. I. H. Riedel-Kruse, A. Hilfinger, J. Howard, F. Jülicher, How molecular motors shape the flagellar beat. *HFSP J.* **1**, 192–208 (2007). doi:10.2976/1.2773861 Medline

16. K. Y. Wan, R. E. Goldstein, Rhythmicity, recurrence, and recovery of flagellar beating. *Phys. Rev. Lett.* **113**, 238103 (2014). doi:10.1103/PhysRevLett.113.238103 Medline

17. J. Alper, V. Geyer, V. Mukundan, J. Howard, Reconstitution of flagellar sliding. *Methods Enzymol.* **524**, 343–369 (2013). doi:10.1016/B978-0-12-397945-2.00019-6 Medline

18. Materials and methods are available as supplementary materials on *Science* Online.

19. S. R. Aragon, R. Pecora, Dynamics of wormlike chains. *Macromolecules* **18**, 1868–1875 (1985). doi:10.1021/ma00152a014

20. R. Ma, G. S. Klindt, I. H. Riedel-Kruse, F. Jülicher, B. M. Friedrich, Active phase and amplitude fluctuations of flagellar beating. *Phys. Rev. Lett.* **113**, 048101 (2014). doi:10.1103/PhysRevLett.113.048101 Medline

21. R. P. Feynman, R. B. Leighton, M. Sands, *The Feynman Lectures on Physics*, vol 1. (Addison-Wesley, Reading, MA, 1966).

22. K. Sekimoto, Kinetic characterization of heat bath and the energetics of thermal ratchet models. *J. Phys. Soc. Jpn.* **66**, 1234–1237 (1997). doi:10.1143/JPSJ.66.1234

23. C. E. Shannon, W. Weaver, *The Mathematical Theory of Communication* (Univ. of Illinois Press, Urbana, 1949).

24. V. Singla, J. F. Reiter, The primary cilium as the cell's antenna: Signaling at a sensory organelle. *Science* **313**, 629–633 (2006). doi:10.1126/science.1124534 Medline

25. C. Battle, C. M. Ott, D. T. Burnette, J. Lippincott-Schwartz, C. F. Schmidt, Intracellular and extracellular forces drive primary cilia movement. *Proc. Natl. Acad. Sci. U.S.A.* **112**, 1410–1415 (2015). doi:10.1073/pnas.1421845112 Medline

26. B. G. Barnes, Ciliated secretory cells in the pars distalis of the mouse hypophysis. *J. Ultrastruct. Res.* **5**, 453–467 (1961). doi:10.1016/S0022-5320(61)80019-1 Medline

27. D. Mizuno, C. Tardin, C. F. Schmidt, F. C. Mackintosh, Nonequilibrium mechanics of active cytoskeletal networks. *Science* **315**, 370–373 (2007). doi:10.1126/science.1134404 Medline

28. C. P. Brangwynne, G. H. Koenderink, F. C. Mackintosh, D. A. Weitz, Nonequilibrium microtubule fluctuations in a model cytoskeleton. *Phys. Rev. Lett.* **100**, 118104 (2008). doi:10.1103/PhysRevLett.100.118104 Medline

29. I. Antoniades, P. Stylianou, P. A. Skourides, Making the connection: Ciliary adhesion complexes anchor basal bodies to the actin cytoskeleton. *Dev. Cell* **28**, 70–80 (2014). doi:10.1016/j.devcel.2013.12.003 Medline

30. W. F. Marshall, Basal bodies: Platforms for building cilia. *Curr. Top. Dev. Biol.* **85**, 1–22 (2008). doi:10.1016/S0070-2153(08)00801-6 Medline

31. J. Prost, J. F. Joanny, J. M. Parrondo, Generalized fluctuation-dissipation theorem for steady-state systems. *Phys. Rev. Lett.* **103**, 090601 (2009). doi:10.1103/PhysRevLett.103.090601 Medline

32. C. Bustamante, J. Liphardt, F. Ritort, The nonequilibrium thermodynamics of small systems. *Phys. Today* **58**, 43–48 (2005). doi:10.1063/1.2012462

33. G. E. Crooks, Entropy production fluctuation theorem and the nonequilibrium work relation for free energy differences. *Phys. Rev. E Stat. Phys. Plasmas Fluids Relat. Interdiscip. Topics* **60**, 2721–2726 (1999). doi:10.1103/PhysRevE.60.2721 Medline

34. C. Jarzynski, Nonequilibrium equality for free energy differences. *Phys. Rev. Lett.* **78**, 2690–2693 (1997). doi:10.1103/PhysRevLett.78.2690

35. J. Liphardt, S. Dumont, S. B. Smith, I. Tinoco Jr., C. Bustamante, Equilibrium information from nonequilibrium measurements in an experimental test of Jarzynski's equality. *Science* **296**, 1832–1835 (2002). doi:10.1126/science.1071152 Medline

36. U. Seifert, Entropy production along a stochastic trajectory and an integral fluctuation theorem. *Phys. Rev. Lett.* **95**, 040602 (2005). doi:10.1103/PhysRevLett.95.040602 Medline

37. R. Ma, G. S. Klindt, I. H. Riedel-Kruse, F. Jülicher, B. M. Friedrich, Active phase and amplitude fluctuations of flagellar beating. *Phys. Rev. Lett.* **113**, 048101 (2014). doi:10.1103/PhysRevLett.113.048101 Medline

38. K. Y. Wan, R. E. Goldstein, Rhythmicity, recurrence, and recovery of flagellar beating. *Phys. Rev. Lett.* **113**, 238103 (2014). doi:10.1103/PhysRevLett.113.238103 Medline

39. E. M. Purcell, Life at low reynolds number. *Am. J. Phys.* **45**, 3–11 (1977). doi:10.1119/1.10903

40. H. Sillescu, R. Bohmer, G. Diezemann, G. Hinze, Heterogeneity at the glass transition: What do we know? *J. Non-crystalline Solids* **307-310**, 16–23 (2002). doi:10.1016/S0022-3093(02)01435-7

41. K. Kim, S. Saito, Multi-time density correlation functions in glass-forming liquids: Probing dynamical heterogeneity and its lifetime. *J. Chem. Phys.* **133**, 044511 (2010). doi:10.1063/1.3464331 Medline

42. C. P. Brangwynne, G. H. Koenderink, F. C. Mackintosh, D. A. Weitz, Nonequilibrium microtubule fluctuations in a model cytoskeleton. *Phys. Rev. Lett.* **100**, 118104 (2008). doi:10.1103/PhysRevLett.100.118104 Medline

43. P. Bursac, G. Lenormand, B. Fabry, M. Oliver, D. A. Weitz, V. Viasnoff, J. P. Butler, J. J. Fredberg, Cytoskeletal remodelling and slow dynamics in the living cell. *Nat. Mater.* **4**, 557–561 (2005). doi:10.1038/nmat1404 Medline

44. G. Massiera, K. M. Van Citters, P. L. Biancaniello, J. C. Crocker, Mechanics of single cells: Rheology, time dependence, and fluctuations. *Biophys. J.* **93**, 3703–3713 (2007). doi:10.1529/biophysj.107.111641 Medline

45. J. Alper, V. Geyer, V. Mukundan, J. Howard, Reconstitution of flagellar sliding. *Methods Enzymol.* **524**, 343–369 (2013). doi:10.1016/B978-0-12-397945-2.00019-6 Medline

46. C. Leduc, F. Ruhnow, J. Howard, S. Diez, Detection of fractional steps in cargo movement by the collective operation of kinesin-1 motors. *Proc. Natl. Acad. Sci. U.S.A.* **104**, 10847–10852 (2007). doi:10.1073/pnas.0701864104 Medline

47. F. Ruhnow, D. Zwicker, S. Diez, Tracking single particles and elongated filaments with nanometer precision. *Biophys. J.* **100**, 2820–2828 (2011). doi:10.1016/j.bpj.2011.04.023 Medline

48. S. R. Aragon, R. Pecora, Dynamics of wormlike chains. *Macromolecules* **18**, 1868–1875 (1985). doi:10.1021/ma00152a014

49. C. Battle, C. M. Ott, D. T. Burnette, J. Lippincott-Schwartz, C. F. Schmidt, Intracellular and extracellular forces drive primary cilia movement. *Proc. Natl. Acad. Sci. U.S.A.* **112**, 1410–1415 (2015). doi:10.1073/pnas.1421845112 Medline

50. C. Battle, L. Lautscham, C. F. Schmidt, Differential interference contrast microscopy using light-emitting diode illumination in conjunction with dual optical traps. *Rev. Sci. Instrum.* **84**, 053703 (2013). doi:10.1063/1.4804597 Medline

51. G. Danuser, P. T. Tran, E. D. Salmon, Tracking differential interference contrast diffraction line images with nanometre sensitivity. *J. Microsc.* **198**, 34–53 (2000). doi:10.1046/j.1365-2818.2000.00678.x Medline

52. D. Sage, F. R. Neumann, F. Hediger, S. M. Gasser, M. Unser, Automatic tracking of individual fluorescence particles: Application to the study of chromosome dynamics. *IEEE Trans. Image Process.* **14**, 1372–1383 (2005). doi:10.1109/TIP.2005.852787 Medline

53. E. A. Schwartz, M. L. Leonard, R. Bizios, S. S. Bowser, Analysis and modeling of the primary cilium bending response to fluid shear. *Am. J. Physiol.* **272**, F132–F138 (1997). Medline

54. Y. N. Young, M. Downs, C. R. Jacobs, Dynamics of the primary cilium in shear flow. *Biophys. J.* **103**, 629–639 (2012). doi:10.1016/j.bpj.2012.07.009 Medline